A Magnetic Field Gradiometer based on the Laser Helium Optically Pumped Magnetic Field Sensors

Chao Wang, Zhijian Zhou, Defu Cheng and Jie Zhang*
College of Instrumentation and Electrical Engineering, Jilin University, Changchun, China

Abstract—When the ratio of the background magnetic field value to the measured magnetic anomaly value is too large, it becomes very difficult for the surveyor to delineate and interpret the magnetic anomaly. Therefore, the measurement of magnetic gradient is particularly important. In this paper, a magnetic field gradiometer based on laser helium optically pumped magnetic sensors is developed. The main contents of the paper include:(1) operating principle of laser helium optically pumped magnetic sensor, (2) program of magnetic field gradiometer based on laser helium optically pumped magnetic sensors, (3) sensor laser source, (4) excitation technology of ^{4}He cell, (5) sensor magnetic signal detection technology. Finally, the performance of the magnetic field gradiometer is tested. The sensitivity of the two sensors was calculated to be 2.65pT/Hz$^{1/2}$ @1Hz and 3.59pT/ Hz$^{1/2}$ @1Hz respectively. By comparing with the theoretical value of magnetic field and the data of Cs-3, it is proved that the gradiometer based on laser helium optically pump magnetometers has good practicability.

Keywords—gradiometer; laser; helium excitation; signal detection.

I. INTRODUCTION

Magnetic field is a basic physical quantity, which contains a lot of environmental information that cannot be observed directly. With the discovery of various magnetic phenomena in people's production and life, more and more attention has been paid to the measurement of magnetic field [1].

Laser optically pumped magnetic field sensor is a kind of high precision magnetic measuring instrument. The magnetic sensitive materials of these sensors mainly include alkali metal (rubidium, cesium, potassium, etc.) and helium. Compared with alkali metals, helium does not need to be heated and kept warm during the measurement process, thus consumes less power [2]. The fundamental physics of laser helium optically pumped magnetic field sensor are the Zeeman splitting and magnetic resonance (NMR) [3,4].

In geophysical exploration, initially, surveyors were only concerned with the total magnetic field strength, which is what we call the magnetic field scalar value. Scalar values are isotropic and are fundamental properties of magnetic fields [5].

Due to the complexity of practical application scenarios and the increasing number of interference factors, the scalar value of the magnetic field will be annihilated in the magnetic field noise [6,7]. When the ratio of the background magnetic field value to the measured magnetic anomaly value is too large, it becomes very difficult for the surveyor to delineate and interpret the magnetic anomaly. But, if the gradient values are measured, the geomagnetic field and magnetic noise can be effectively filtered out to highlight the magnet under test. The total magnetic field gradient measurement makes the data types of magnetic detection more diversified, and it significantly improved the ability to obtain and analyze magnetic anomaly.

Nowadays, magnetic gradient measurement technology has been widely used in various fields of high precision magnetic measurement, including geophysical exploration, national defense and biomedicine [8,9].

The foundation of total field gradient measurement is a high precision magnetic measuring instrument. Therefore, a magnetic field gradiometer based on laser helium optically pumped sensors is introduced in this paper. The program of gradiometer, laser source, excitation energy source of cell and signal detection technology were studied. Finally, the performance of the gradiometer is tested.

II. OPERATING PRINCIPLE AND PROGRAM OF GRADIOMETER

A. Operating principle and sensitivity of optically pumped magnetic field sensor

The helium optically pumped magnetic field sensor has a glass cell filled with ^{4}He atoms. In a magnetic field, ^{4}He atoms undergo the Zeeman effect, in which the Zeeman-splitted level formed according to the value of *M* (the magnetic quantum number of ^{4}He atoms). The energy interval between adjacent Zeeman-splitted level is proportional to the strength of the external magnetic field ***B***. *1^{1}S^0* represents the ground state of ^{4}He atomic energy, *2^{3}S^1* represents the metastable state of ^{4}He atomic energy, and *2^{3}P^1* represents one of the excited states of ^{4}He atomic energy, as shown in **Fig.1**. ^{4}He atoms at *1^{1}S^0* need to be stimulated by a discharge to cause collisions between electrons, absorbing energy in the process to jump to *2^{3}S^1*. ^{4}He atoms at *2^{3}S^1* and *2^{3}P^1* are active [10-13].

Providing circularly polarized light to ^{4}He atoms, light energy induces ^{4}He atoms evenly distributed in *2^{3}S^1* to transition to higher energy levels, the transition rule is *ΔM = +1* , this phenomenon is called optical pumping. At the

same time, due to relaxation, the ^{4}He atoms after transition will stay for a short time and then fall back to the lower energy level with equal probability. The transition between energy levels in two directions is cyclic, as shown in **Fig.1**. Finally, the optical pumping and relaxation achieve a dynamic equilibrium, with the ^{4}He atoms aligned in a magnetic direction [13,14]. This dynamic process is called the polarization of ^{4}He atoms. During polarization, ^{4}He atoms need to absorb light energy.

Fig. 1. Transitions in the process of atomic polarization and depolarization.

Helmholtz coil were used to apply alternating magnetic fields to ^{4}He atoms. When the frequency of the alternating magnetic fields is equal to the Larmor frequency, NMR occurs and the depolarization process is induced [15-17]. In the

process of depolarization, transition between adjacent energy levels causes the magnetic moment of atoms to lose its orientation, as shown in **Fig.1**.

The intensity of light passing through ^{4}He atoms is monitored by photodetector. The signal produced by the photodetector is called the magnetic resonance signal. Depolarized ^{4}He atoms need to reabsorb light energy, so, we get the magnetic resonance point when the light intensity is the weakest.

The principle expression of magnetic field measurement is:

$$B(nT) = \frac{v_J(Hz)}{28.02356} \tag{1}$$

Sensitivity is the fundamental index of sensor, usually, the sensitivity of optically pumped magnetic sensor is expressed by:

$$\delta B = \frac{\Delta f}{\Delta S / N} \tag{2}$$

Δf is the resonance signal linewidth, which is the frequency difference between the maximum slope point and the minimums slope point in the signal curve. *ΔS* is the resonance signal amplitude. *N* is the noise power spectrum density of resonance signal.

B. Program of gradiometer

According to the operating principle, the magnetic field gradiometer based on laser helium optically pumped magnetic field sensors is a kind of precision instrument which integrates the design of optics, circuit and mechanical structure. The
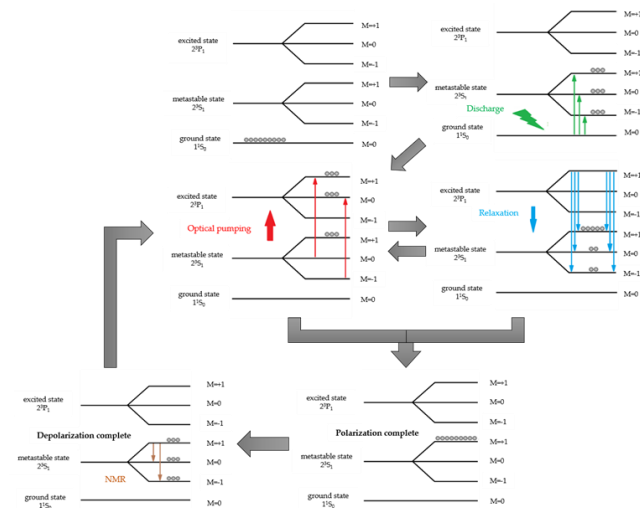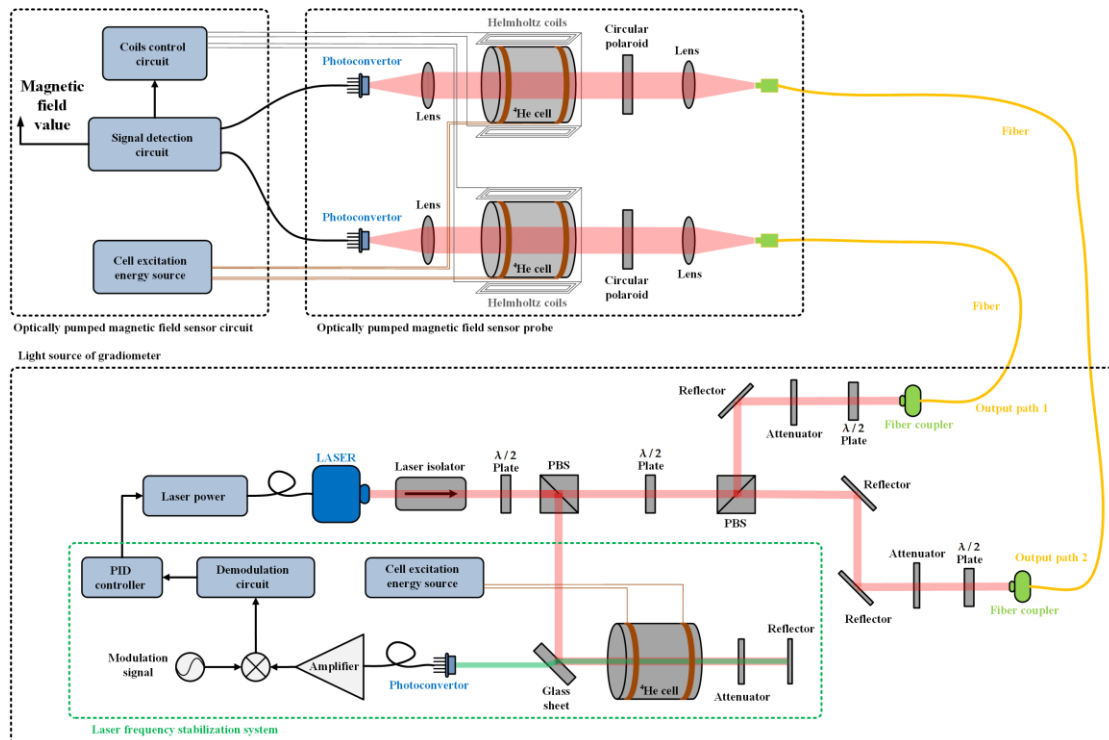

Fig. 2. Program of magnetic field gradiometer.

program of magnetic field gradiometer is shown in **Fig.2.**

The magnetic field values measured by the two sensors are B_A and B_B respectively. The distance of the two sensors is ΔL. The value of the gradient is (3).

$$\frac{dB}{dL} = \frac{B_A - B_b}{\Delta L} \qquad (3)$$

The gradiometer mainly consists of laser light source, optically pumped magnetic field sensor probe and sensor circuit. The laser light source can be subdivided into laser power, laser frequency stabilization system, spectral optical path and coupling optical path. The optically pumped magnetic field sensor probe comprises ^{4}He cell, Helmholtz coils, absorption path and photoconverter. The sensor circuit includes the ^{4}He cell excitation energy source, the signal detection circuit and the coils control circuit.

III. OPTICAL TECHNOLOGY OF GRADIOOMETER

A. Laser source and laser frequency stabilization system

According the wavelength of transition line corresponding to ^{4}He atoms polarization, we select a DFB laser diode whose wavelength range covers 1083.207nm. The key factors influencing the wavelength of DFB laser include temperature and current [13,18].

The influence of temperature on the laser wavelength is as follows:

$$\lambda = \lambda_0 + k_1(T - T_0) \qquad (4)$$

The influence of current on the laser wavelength is as follows:

$$\lambda = \lambda_0 + k_2(I - I_0) \qquad (5)$$

λ (nm) is the theoretical wavelength of laser, λ_0(nm) is the central wavelength of laser, k_1 (nm/°C) is the tuning coefficient of temperature to wavelength, k_2 (nm/mA) is the tuning coefficient of the current to wavelength, T (°C) is the actual temperature, I (mA) is the actual current, T_0 (°C) is the temperature threshold, I_0 (mA) is the current threshold.

EYP-DFB-1083-00080-1500-BFW01-0002 laser diode from Eagleyard company was selected. The main parameters were k_1=0.06nm/°C, k_2=0.003nm/mA, T_0=25°C, I_0=70mA, λ_0=1083nm at room temperature. According to (4) and (5), wavelength at 1083.207nm needs $I \approx$139mA, $T \approx$28.45°C.

As shown in **Fig.2**, a closed-loop feedback system based on the saturated absorption spectrum of ^{4}He atoms was constructed to stabilize the laser frequency. The glass sheet, attenuator and reflector cause the laser beams that shoot into the ^{4}He cell in opposite directions but take roughly the same path. Mixing the photoconverter signal and the sine modulation signal. Differential error signal is obtained by phase-locked amplification, filters, and demodulators. Then the PID regulator adjusts the differential error signal to the appropriate feedback gain and sends it back to the laser power to stabilize the laser frequency.

Also as shown in **Fig.2**, laser beam passes through the laser isolator, it splits into two parts via $\lambda/2$ plate and PBS (Polarization Beam Splitter). One beam is applied to the saturation absorption spectrum, another beam bundle splits again, through $\lambda/2$ plate and PBS. The rotatable $\lambda/2$ plate and attenuator can adjust the laser intensity. The laser beams through the $\lambda/2$ plate are linearly polarized light, and they are coupled into a single-mode polarization-preserving fiber for output.

The theoretical maximum output power of DFB laser diode selected for the light source is 90mW. The laser isolator was selected from Thorlabs IO-5-1083-VLP, and its forward transmission efficiency was about 92%. $\lambda/2$ plate was selected from Thorlabs WPV10-1083, and its forward transmission efficiency is greater than 96%. PBS was selected from Thorlabs PBS053, and its transmission efficiency was more than 90%, reflection efficiency was more than 99.5%. Therefore, the theoretical maximum power value of the beam before the second splitting is $P_t = 90 \Box 92\% \Box 96\% \Box 90\% \Box 96\% \approx 68mW$. Since the transmission and reflection efficiency of the PBS are different, the two beams after splitting also have power deviation. By rotating the attenuator, the power of two beams can be ensured to be consistent.

According to the light path shown in **Fig.2**, the anti-vibration mechanical structure shown in **Fig.3(a)** was designed. Non-magnetic pure aluminum was used, and the size of light source is 50cm*40cm*15cm (length * width * height), the weight is about 15kg.
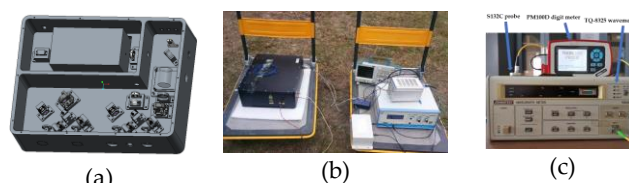

| (a) | (b) | (c) |

Fig. 3. (a) Light source structure design. (b) Performance test of light source outdoor. (c) Light source testing equipment

TABLE I. Partial parameters of the beam

	Output path 1	Output path 2
Power adjusTABLE range	1mW---23mW	1mW---21mW
Power fluctuation range	< ±0.01mW	< ±0.01mW
Power fluctuation percentage error	<20‰	< 20‰
Central value of wavelength	1083.207nm	1083.207nm
Wavelength fluctuation	<±0.001nm	<±0.001nm
Wavelength fluctuation percentage error	< 0.002‰	< 0.002‰

The finished light source and its outdoor test status are shown in **Fig.3(b)**. The beam quality of the light source is measured by the wavemeter and optical power meter, the test equipment is shown in **Fig.3(c)**. Partial parameters of the beam are shown in **TABLE I**.

The measured optical power range of output path 1 is 1mW-- 23mW, the optical power range of output path 2 is 1mW-- 21mW. The actual difference between transmission and

reflection efficiency of the PBS is about 4.5%, which is meet design expectations. The efficiency of the coupler, $\eta = (21+23)/68 \approx 65\%$, also meeting the design expectations. Within 30 minutes, the optical power fluctuation of both output beams was less than ±0.01mW, the percentage error of optical power fluctuation within the adjustable power range shall not exceed 20‰. Within 30 minutes, the wavelength fluctuation was less than ±0.001nm, and the percentage error of wavelength fluctuation was less than 0.002‰.

The laser light source is powered by ±18V DC power supply. When it works stably, the positive power supply current is about 300mA, the negative power supply current is about 200mA, and the overall power consumption is about 9W.

B. Structure design of sensor probe

The beam output by single-mode polarization-maintaining fiber is linearly polarized light with divergence Angle, therefore, it is necessary to collimate the beam first in the optical path of magnetic sensor probe. After collimating, the beam is transformed into circularly polarized light by circular polaroid.

The optical path design of the magnetic sensor probe is shown in **Fig.2**. The light beam is collimated by a convex lens, and finally focused by a convex lens into the photoconverter. The lens was selected from Thorlabs LA252-C, with a focal length of 25.4mm. Circular polaroid was selected from Thorlabs CP1L-1083-SP. Using PLA (polylactide) material, 3D printing technology was used to make the non-magnetic magnetic sensor. In the manufacture of sensors, the optical elements should be coaxial, the fiber output joint and photodiode photosensitive surface should be placed near the focal point of the lens.
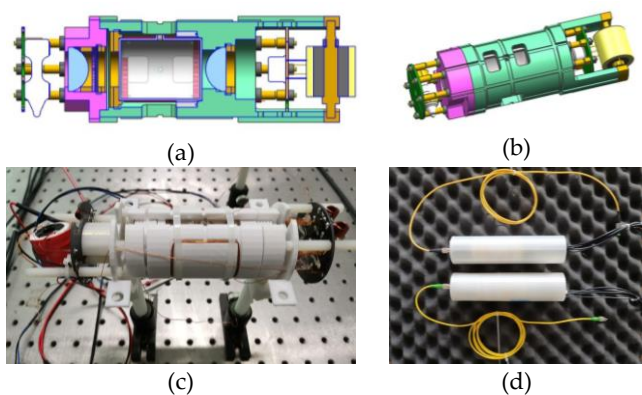

Fig. 4. (a) (b) Structure design of magnetic sensor probe. (c) The inner structure of probe. (d) The completed probes

The structure design of the magnetic sensor probe is shown in **Fig.4 (a)** and **Fig.4 (b)**. The inner structure of the probe is shown in **Fig.4 (c)**. The completed dual-channel magnetic sensor probes are shown in **Fig.4 (d)**. The probe is cylindrical in shape, with a diameter of 54mm, a length of 200mm and the weight of a single probe is about 1kg.

IV. EXCITATION ENERGY SOURCE OF ⁴HE CELL

A. Program of excitation energy source

The cell is a cylindrical sealed glass chamber filled with ⁴He. Since ⁴He is an inert gas, the cell needs to accept the energy to make the ⁴He atoms in the ground state jump to metastable state. After transition, ⁴He atoms have "activity" to make magnetic measurements. This process of activating ⁴He atoms in the cell is called the excitation.

According to the gas discharge theory, the initial state of ⁴He atom in the excitation process belongs to the non-self-sustaining discharge, while the stable state belongs to the self-sustaining discharge. The phenomenon of the transition from the non-self-sustaining discharge to the self-sustaining discharge is called the breakdown of the gas [19,20]. The breakdown happens instantaneously if the ⁴He atoms gain a lot of energy instantaneously. Once in a self-sustaining state, ⁴He atoms need only a small amount of energy to sustain the discharge. Therefore, the design scheme of the excitation energy source of ⁴He cell is shown in **Fig.5**.
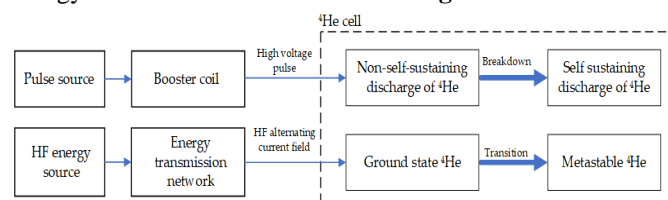

Fig. 5. Program of the ⁴He cell excitation energy source

The high voltage pulse caused a huge voltage difference between the two external electrodes over the cell instantaneously. After the voltage difference exceeds the breakdown threshold, ⁴He is broken down and enters the self-sustaining discharge state, then, the cell presents stable resistance characteristics. Meanwhile, HF energy source provides an alternating current field to the cell by another set of external electrodes, providing the energy needed to sustain the self-sustaining discharge of ⁴He. The energy transmission network can match the impedance between the energy source and cell to ensure the high energy transmission efficiency.

B. High voltage excitation technology

According to Paschen law [21], the product of ⁴He pressure P_{He} and discharge gap d_{He} can be drawn as Paschen curve with ⁴He breakdown voltage V_{He}. When the value of $P_{He} \square d_{He}$ is small, V_{He} decreases exponentially with the increase of $P_{He} \square d_{He}$. When the value of $P_{He} \square d_{He}$ is large, V_{He} increases slowly and linearly with the increase of $P_{He} \square d_{He}$. The intersection of two curves is called the minimum breakdown voltage. According to the data, when $P_{He} \square d_{He} = 533.3 \text{cm}/\text{Pa}$, the minimum breakdown voltage of ⁴He is 156V.

The cell is cylindrical, about 4cm in diameter and 5cm in length, with a ⁴He-filled pressure of about 100Pa. The external high-voltage electrode was installed symmetrically at both ends of the cell, and the distance between them, namely the discharge gap, was about 3cm. The $P_{He} \square d_{He}$ of cell is about

300cm/Pa, and the breakdown voltage of ^{4}He in the cell is estimated to be about 1.5kV based on the Paschen curve.

A tunable pulse source based on multivibrator and booster coil is designed. With trigger switch control, the pulse source provides a transient periodic pulse for cell. The circuit design is shown in **Fig.6**.
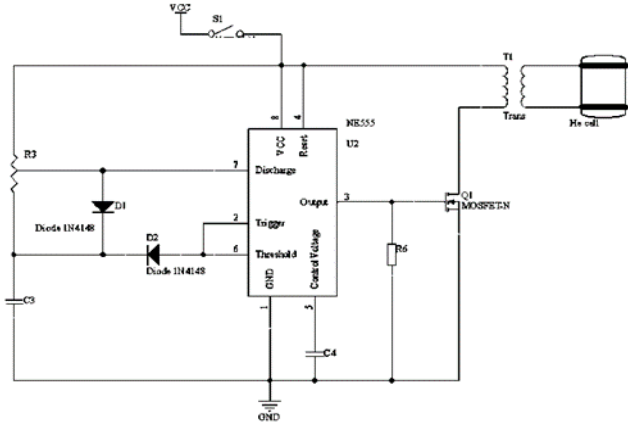

Fig.6. High voltage pulse source based on multivibrator

R_3 and C_3 can adjust the period of pulse output of the oscillator. R_3 can be equivalent to resistance R_1 in series between D_1 and the power supply, and R_2 in parallel with D_2. When the power is switched on, the current is charged through R_1 to C_3, when the power is disconnected, C_3 discharges through R_2. Suppose the pulse duty cycle is Q_0, then:

$$Q_0 = \frac{R_1 C_3 \Box ln2}{R_1 C_3 \Box ln2 + R_2 C_3 \Box ln2} = \frac{R_1}{R_1 + R_2} \quad (6)$$

The V_{pp} of the pulse voltage are consistent with the supply voltage, is 12V. The pulse is fed into the booster coil after power amplification. Since the ^{4}He breakdown voltage in cell is about 1.5kV, and in order to reduce the adverse effect on the magnetic measurement, a hollow boost coil with a ratio of primary to secondary turns which is 20:12000 was designed. For the same reason, the pulse frequency should be as far away as possible from the modulation frequency of Helmholtz coils. The pulse frequency is set to 20kHz when $R_3 = 2k\Omega$ and $C_3 = 36nF$.

TINA software developed by Texas Instruments was used to simulate the multivibrator. According to (5), when the ratio of R_1 and R_2 is 1:9, the duty cycle of the periodic pulses is about 10%, the simulation result is shown in **Fig.7(a)**, frequency of signal is about 20kHz. The measured waveform of circuit is shown in **Fig.7(b)**, the duty cycle of the signal is about 9.05%, and the frequency is about 20.67kHz. The high voltage pulse source is in line with the design expectation.
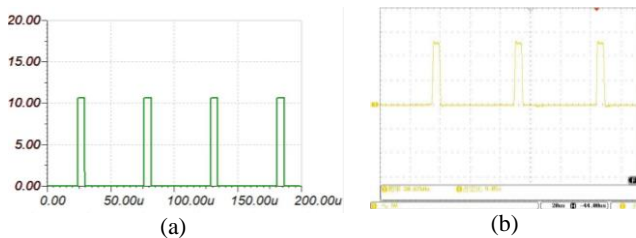

(a)   (b)

Fig.7. (a) Simulation result of TINA. (b) Measured waveform

C. High frequency excitation technology

The ^{4}He cell is connected to the excitation circuit by coaxial cable. Therefore, it is necessary to design a HF energy source circuit with MOSFET power amplifier, and an impedance matching network. Drawing on the experience in the field of gas discharge lamp [19,20], a 50MHz HF energy source program was designed, as shown in **Fig.8**.
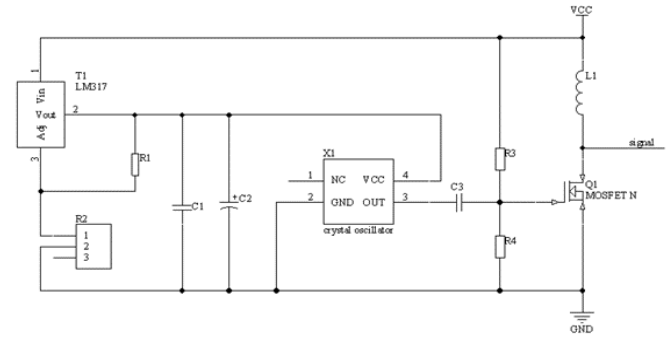

Fig.8. HF energy source circuit

The constant temperature crystal oscillator provides a stable 50MHz output. The common source amplifier is designed by using MOSFET. The partial voltage offset circuit composed of R_3 and R_4 can provide the appropriate gate source voltage V_{GS} for the MOSFET. Select MITSUBISHI RD06HVF1 high frequency MOSFET, whose on voltage $V_T = 4V$, the circuit operating voltage $Vcc = 12V$. When the values of R_3 and R_4 are 2kΩ and 1kΩ respectively, $V_{GS} = 8V > V_T$, and the MOSFET can work in the saturated region. The common source power amplifier belongs to class A power amplifier according to the characteristics of the circuit during the waveform cycle.

MOSFET is a voltage control device. In the saturation region, the drain output current i_D and the gate source voltage V_{GS} show a linear relationship within a certain range. Therefore, the HF energy source shown in **Fig.9** is a single-port output network. Typical output power of RD6HVF1 is 6W, circuit power supply $Vcc = 12V$, saturation tube pressure drops $V_{dss} \approx 1V$. According to the maximum power transfer theorem, the load impedance of the maximum output power can be estimated:

$$R_{Ls} = \frac{U_{R_L m}^2}{2P_{omax}} = \frac{(V_{cc} - V_{dss})^2}{2P_{omax}} = \frac{(12-1)^2}{2\Box 6} \approx 10\Omega \quad (7)$$

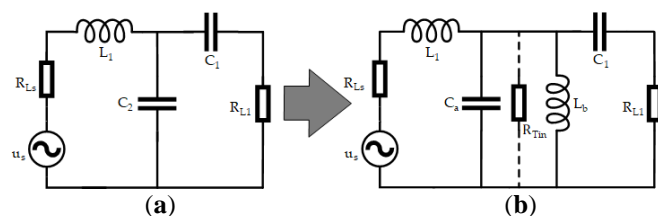(a)   (b)

Fig.9. (a) The T-network design of energy transmitter circuit. (b)

The double L-network equivalent model of T-network.

In the actual process of circuit preparation, the choice of capacitor is simpler than that of inductor, and the error control of capacitor is better than that of inductor. Therefore, the use of inductance should be minimized in circuit design. Design the impedance matching T-network as shown in **Fig.9(a)**. C_2 in the circuit can be divided into two parallel components C_a and L_b, T-network can be equivalent to a double L-network model, and an imaginary resistor R_{Tin} is inserted in the middle [22]. The double L-network equivalent model is shown in **Fig.9(b)**.

According to (7), the T-network source impedance is $R_{LS} = 10\Omega$. Since the coaxial cable impedance is 50Ω, the load impedance is $R_{LI} = 50\Omega$, $R_{LI} > R_{Ls}$. The matching conditions are $R_{Tin} > R_{Ls}$ and $R_{Tin} > R_{LI}$. In **Fig.9(b)**, the quality factor of L-network nodes composed of L_I and C_a is defined as Q_{TI}, the quality factor of L-network nodes composed of L_b and C_I is defined as Q_{T2}, then:

$$Q_{TI} = \sqrt{\frac{R_{Tin}}{R_{Ls}} - 1} \qquad (8)$$

$$Q_{T2} = \sqrt{\frac{R_{Tin}}{R_{LI}} - 1} \qquad (9)$$

The passband width of T-network is determined by Q_{TI} and Q_{T2}. Since $R_{LI} > R_{Ls}$, so $Q_{TI} > Q_{T2}$, it is necessary to select Q_{TI} to calculate the parameters from the source impedance. The on-load quality factor of the circuit is $Q_{TL} = Q_{TI} / 2$, the 3dB passband width of T-network is:

$$BW_{T0.7} \approx \frac{f_0}{2Q_{TL}} \qquad (10)$$

After calculation, it can be obtained that:

$$R_{Tin} = (1 + Q_{TI}^2)R_{Ls} \qquad (11)$$

$$L_I = Q_{TI} \square R_{Ls} \qquad (12)$$

$$C_I = Q_{T2} \square R_{LI} \qquad (13)$$

Since C_a and L_b are in parallel to form C_2, and there are $C_a = R_{Tin} / Q_{TI}$, $L_b = R_{Tin} / Q_{T2}$, so:

$$C_2 = \frac{\left\lfloor \left(1 + Q_{TI}^2\right)R_{Ls} / Q_{TI} \right\rfloor \square \left\lfloor \left(1 + Q_{TI}^2\right)R_{Ls} / Q_{T2} \right\rfloor}{\left(1 + Q_{TI}^2\right)R_{Ls} / Q_{TI} + \left(1 + Q_{TI}^2\right)R_{Ls} / Q_{T2}} \qquad (14)$$

The T-network has the function of frequency selection. According to the definition of narrow-band filter, the target 3dB passband width of T-network is set to 2.5MHz. Substitute the data into (8) to (14) for calculation. Ideally, L_I=636.62nH, C_I=7.15pF, C_a=15.9pF, L_b=1434nH.

Agilent's ADS (Advanced design System) was used to conduct simulation experiments. In the simulation experiment,

S parameter is used to measure the performance of matching network. Ideally, because $2\pi f_0 C_a > 1 / 2\pi f_0 L_b$, the parallel circuits of C_a and L_b are capacitive, and C_2=8.815pF is obtained through design optimization. The simulation results are shown in **Fig.10**. At 50MHz, $S_{11} = -66.232dB$, $S_{21} = 0dB$, and 3dB passband width $BW_{T0.7} \approx 4.4MHz$.
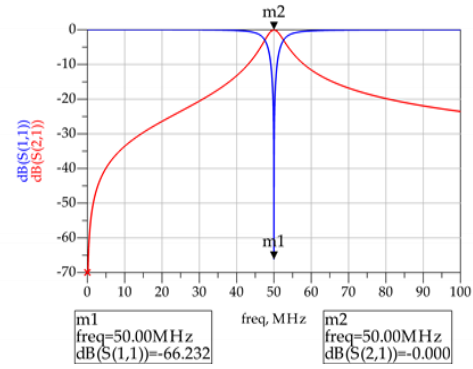

Fig.10. The simulation results of T-network.

According to the simulation experiment, the excitation circuit of ⁴He cell is made, as shown in **Fig.11(a)**. The ammeter is used to measure the instantaneous working current $I_{start} \approx 1A$ and the stable working current $I_{work} \approx 500mA$ respectively. Since the supply voltage is 12V, the instantaneous power of the circuit starting is $P_{start} \approx 12W$, and the power $P_{work} \approx 6W$ in the stable working state. NISSEI RS-70 standing-wave meter and 50Ω virtual load were used to test the actual output power, the maximum value is $P_{out} \approx 2W$.
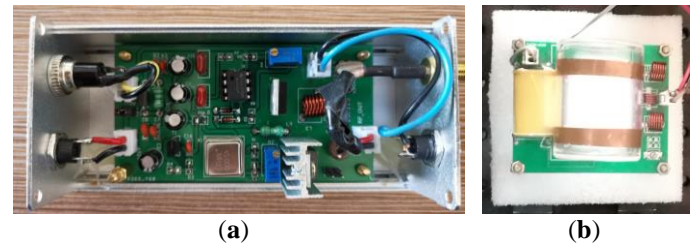

(a)   **(b)**

Fig.11. (a)The excitation energy source circuit. (b) ⁴He cell has been ignited.

It can be calculated that the energy transfer efficiency of HF energy source is $\eta_P = 2W / 6W \approx 33.3\%$. Since the theoretical maximum energy transfer efficiency of class A power amplifier is 50%, the energy transfer efficiency of e T-network is $\eta_{PO} > 67\%$, $S_{21} > -3.5dB$, close to the empirical guide value -3dB for matching network design. Considering the influence of wiring trend and circuit fabrication process in circuit design, the circuit performance basically conforms to the design expectation.

V. SIGNAL DETECTION SYSTEM

Optically pumped magnetic sensor measurement is a closed-loop feedback regulation process. The signal detection system needs to lock the resonance point. The structure diagram of signal detection system is shown in **Fig.12**. Optical

signal related to the magnetic field is converted into electrical signal by photoconverter. The electrical signal is observed trough A/D convertor transforming to digital after processing of pre-amplifier and band-pass filter. An alternating electric

tuning rules [24]. The forward gain and open-loop gain settings are equal for convenient simulation of the system. and sampling rate is set as 10Hz.

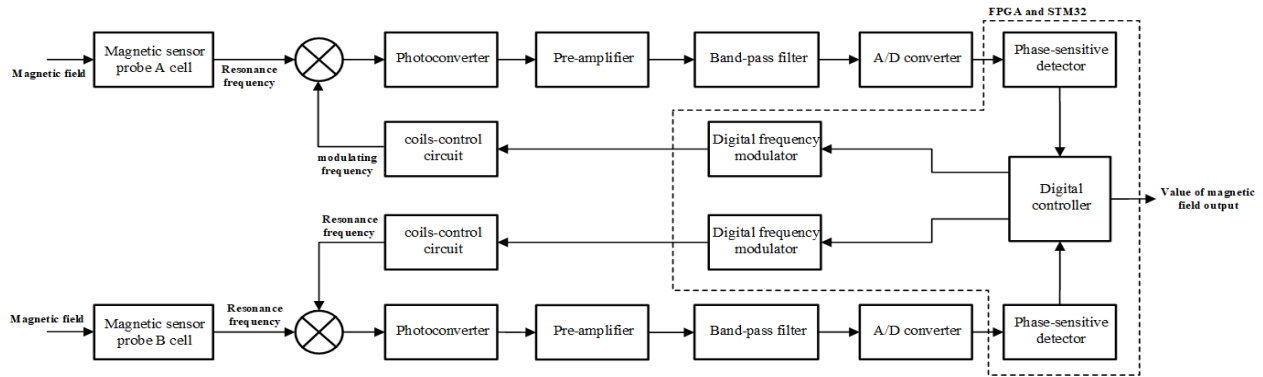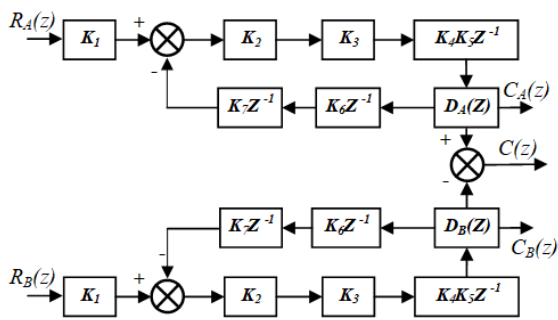Unit Step response simulation was carried out for the ̄e set

Fig. 12. The structure diagram of signal detection system.

field frequency modulator is built in FPGA, and the modulator drives the Helmholtz coils through a circuit. Modulating signal generated by the Helmholtz coils is applied to the cell, forming

Fig.13. The mathematical model of signal detection system.

The mathematical model of signal detection system is shown in **Fig.13**. The closed-loop transfer function of the mathematical model is expressed as (15).

$$H(Z) = \frac{K_1 K_2 K_3 K_4 Z^{-1} D(Z)}{1 + K_2 K_3 K_4 K_5 K_6 Z^{-3} D(Z)} \quad (15)$$

In (15), K_1 is gyromagnetic ratio, K_1=28.02356, K_2 is coefficient of photoelectric to voltage, K_2=0.9×190×1000, K_3 is magnification of pre-amplifier and filter, K_3=10×510×5, K_4 and K_5 are amplification of AD convertor and phase-locked amplifier, respectively, K_4=2^{18}/5, K_5= 1.3563×1.8118. K_6 and K_7 are coefficient of frequency modulator and coils-control circuit, respectively, K_6=(14000×2π×10)/(49999872×2^{48}), K_7=12/3.3. Increment PID is selected and expressed as (16) [23].

$$D(Z) = \lfloor K_P(1 - Z^{-1}) + K_I + K_D(1 - 2Z^{-1} + Z^{-2}) \rfloor (1 + Z^{-1}) \quad (16)$$

Where K_P, K_I and K_D are coefficient of proportional, integral and differential respectively. The calculation result simulated on MATLAB is obtained using Ziegler-Nichols
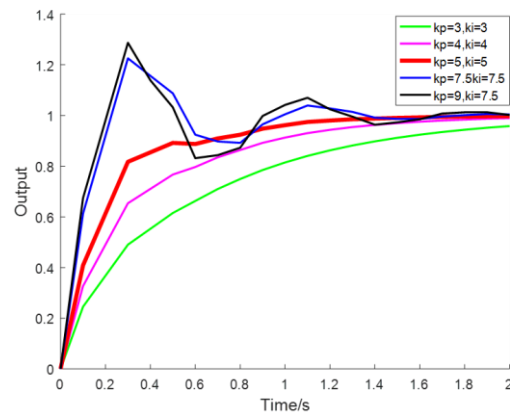
and the results of simulation are shown in the **Fig.14.** It is proved that K_P=5, K_I=5, K_D=0 is reasonable.

Fig.14. The simulation results of unit step response.

On the basis of PID parameters, the working process of optimized frequency modulator is simulated, and experimental results are shown in **Fig.15**. *clk* represents the clock signal of the detection system, *lia* represents the obtained deviation *e(k)*, *pid_clk* represents the clock signal of PID controller, *delta_uk* represents the frequency modulator output signal *f(k)*.
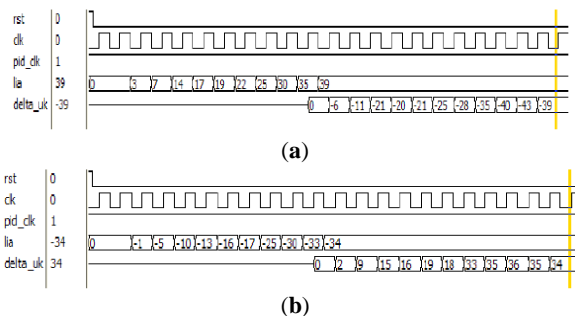

(a)

(b)

Fig.15. Simulation results of modulator (a) Deviation value is positive (b) Deviation value is negative.

The experimental results show that the digital frequency modulator based on the increment PID method can effectively eliminate the modulation frequency and resonance frequency deviation in the signal detection process, system can lock the magnetic resonance point quickly and accurately.

VI. PERFORMANCE OF THE MAGNETIC FIELD GRADIOMETER

A. Test environment and equipment

A theoretical "zero magnetic" space was created by a magnetic field shielding tube shown in **Fig.16(a)**. The tube is a 6-layer structure with aluminum and magnetic conductive permalloy alloy. The attenuation of external geomagnetic field by the tube can reach about 80dB. Test results of magnetic environment in magnetic field shielding tube shown in **Fig.16(c)**. The horizontal axis of **Fig.16(c)** is the distance between the test point and the entrance. The magnetic field fluctuation in the tube is less than 0.1nT.
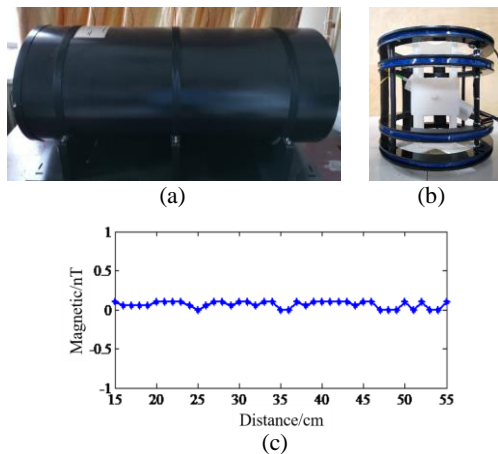

Fig. 16. (a) Magnetic field shielding tube (b) Helmholtz-Maxwell composite coils (c) Test results of magnetic environment in magnetic field shielding tube.

Helmholtz-Maxwell composite coil, are used to create different types of stable magnetic field environments in the magnetic shielding tube, as shown in **Fig.16(b)**. The pair of coils close to each other are Helmholtz coils with a 15cm radius and 217 turns. The pair far apart are Maxwell coils with 15cm radius and 120 turns. The simulate results of coil's performance are shown in **Fig.17**.
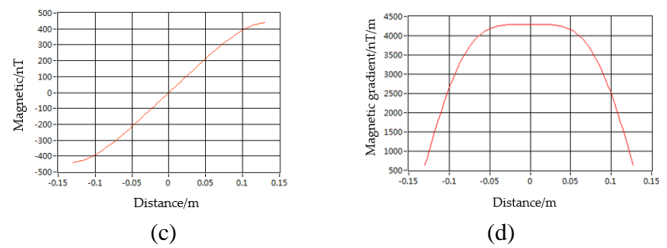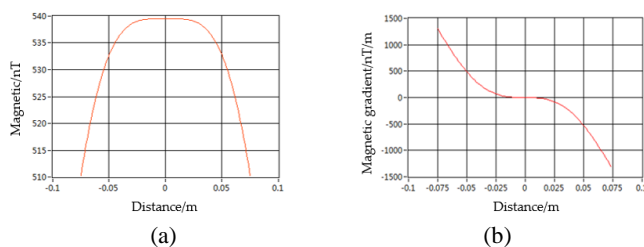

Fig.17. Helmholtz-Maxwell coils simulation results.

The horizontal axis in **Fig.17(a)** and **Fig.17(b)** shows the distance between any point along the Helmholtz coil axis and the center point. The horizontal axis in **Fig.17(c)** and **Fig.17(d)** shows the distance between any point on the axis of Maxwell coil and the center point. The vertical axis in **Fig.17(a)** and **Fig.17(c)** represents the value of the magnetic field at any point along the axis when 1mA current is introduced. The vertical axis in **Fig.17(b)** and **Fig.17(d)** represents the gradient of the magnetic field of the 1mA current.

According to the simulation results, the proportional coefficient of magnetic field to current in the uniform region of Helmholtz coils is about 540nT/mA, and the proportional coefficient of magnetic gradient field to current generated of Maxwell coils is about 3000nT/ m@1mA.

B. Sensitivity of laser ^{4}He optically pumped magnetic field sensor

90mA current is applied to the Helmholtz coils, and the theoretical magnetic field value should be about 48600nT. According to (1), the magnetic resonance frequency is about 1.36MHz. The frequency range of the alternating electric field was set as 0.8MHz-1.8MHz, and the scanning period set as 1s. The signal sampling rate set as 1k.

The two magnetic sensor probes are named probe A and probe B respectively. The test results are shown in **Fig.18 (a)** and **Fig 18.(b)**, respectively. The solid red line and the dotted blue line represent two test results of the same probe. The horizontal axis in **Fig.18** is the number of sampling points, and the corresponding scanning frequency of each sampling interval can be calculated to be about 1000Hz. The vertical axis in **Fig.18** represents the voltage in unit **V**.
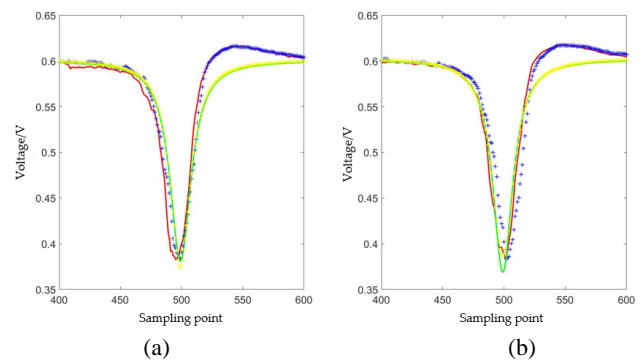

Fig. 18. (a) Resonance signal curve of Probe A. (b) Resonance signal curve of Probe B.

Lorentz line fitting was performed on the test data. Set the fitting model as:

$$y = a - \frac{c}{d + bx^2} \qquad (17)$$

The least square method was used to solve the model parameters. Since the model was nonlinear, the Adam gradient descent optimization method was used to solve the parameters. The number of iterations is 50000, and the parameters are shown in **TABLE II**.

TABLE II. Lorentz line fitting parameters

		a	b	c	d	y MSE
Probe A	Data 1	0.6005	0.0136	0.3246	1.4768	0.00013
	Data 2	0.6015	0.0161	0.3606	1.5829	0.00007
Probe B	Data 1	0.6020	0.0165	0.3724	1.5942	0.00005
	Data 2	0.6033	0.0129	0.3125	1.4430	0.00007

The four groups of parameters were substituted into (17), and the fitting curve was shown in **Fig.19 (a)** and **(b)**. The solid green line represents the fitting curve of two groups data 1, and the yellow dotted line represents the fitting curve of two groups data 2. Take the derivative of (17), $\Delta f = \sqrt{d / 3b}$ and $\Delta S = c / d$. We get four groups of Δf and ΔS are shown in **TABLE III**.

TABLE III. Values of Δf and ΔS

		Δf	ΔS	N
Probe A	Data 1	417nT	220mV	1.33$\mu V/Hz^{1/2}$@1Hz
	Data 2	407nT	228mV	1.55$\mu V/Hz^{1/2}$@1Hz
	Average	**412nT**	**224mV**	**1.44$\mu V/Hz^{1/2}$@1Hz**
Probe B	Data 1	400nT	234mV	2.11$\mu V/Hz^{1/2}$@1Hz
	Data 2	428nT	217mV	1.81$\mu V/Hz^{1/2}$@1Hz
	Average	**414nT**	**226mV**	**1.96$\mu V/Hz^{1/2}$@1Hz**

The dynamic signal analyzer is used to test the noise power spectral density N of the signal. The two probes measure two sets of data respectively, and the results are shown in **Fig. 19 (a)** and **(b)**.
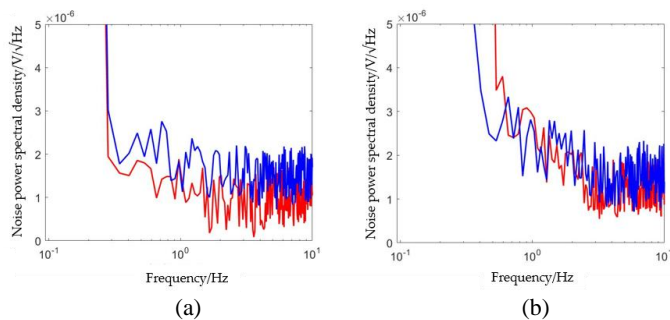

Fig. 19. (a) Noise power spectral density of Probe A. (b) Noise power spectral density of Probe B.

Probe B is higher in N than probe A at 1Hz, as shown in **TABLE III**. The reason is that the components and welding technology of the two probes are different, and the photodiode

installation has position deviation. After averaging the two sets of data, the sensitivity values of the two probes were calculated according to (2). As shown in **TABLE IV**.

TABLE IV. Sensitivity of two probes

	Sensitivity δB
Probe A	2.65$pT/Hz^{1/2}$@1Hz
Probe B	3.59$pT/Hz^{1/2}$@1Hz

C. Performance of gradiometer

Place the two probes in the Helmholtz-Maxwell composite coil at the same time and install at a distance of 10cm. According to the parameters of coil, set the current value into the Helmholtz coil to 75mA, and set the current value into the Maxwell coil to increase in range of 1mA to 10mA with a 1mA step. Theoretically, the two positions where the magnetic sensor is placed will generate a magnetic gradient field in the range of 40350-39000nT and 40650-42000nT, respectively.
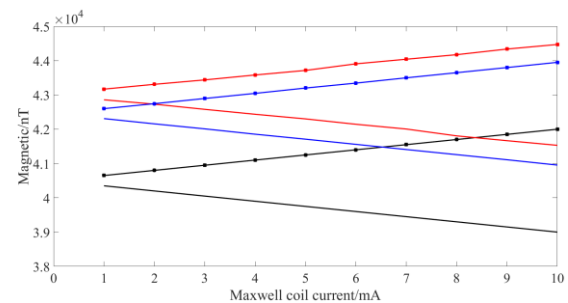

Fig.20. Data of magnetic field gradiometer and Cs-3.

As shown in **Fig.20**, the red solid line and red dot indicate the magnetic field values measured by the two probes of the magnetic field gradiometer, respectively. The solid blue line and the blue dots represent the magnetic field values measured by Cs-3, respectively. Solid black lines and dots represent theoretical values of magnetic fields. According to the values in **Fig.20** and the installation distance of probes, the calculation results of magnetic gradient value are shown in **TABLE V**.

TABLE V. Magnetic gradient value comparison

	theoretical values	Cs-3 values	gradiometer values
1-2mA	3000nT/m	3230nT/m	3240nT/m
2-3mA	3000nT/m	3200nT/m	3220nT/m
3-4mA	3000nT/m	3210nT/m	3230nT/m
4-5mA	3000nT/m	3200nT/m	3210nT/m
5-6mA	3000nT/m	3210nT/m	3220nT/m
6-7mA	3000nT/m	3220nT/m	3230nT/m
7-8mA	3000nT/m	3210nT/m	3210nT/m
8-9mA	3000nT/m	3200nT/m	3200nT/m
9-10mA	3000nT/m	3200nT/m	3200nT/m
average	3000nT/m	3209nT/m	3218nT/m

As shown in **TABLE V**, the values measured by the magnetic field gradiometer and two Cs-3 are slightly larger than the theoretical values of magnetic gradient, because the

deviation between the actual parameters of the coil and the ideal parameters caused by the manufacturing process. But, the measurement results of gradiometer and two Cs-3 are basically the same. In conclusions, the performance of the magnetic field gradiometer based on laser helium optically pumped magnetic field sensors is excellent.

VII. CONCLUSIONS

This paper designed a magnetic field gradiometer based on laser helium optically pumped magnetic field sensors. The sensitivity of two probes was 2.65pT/ Hz$^{1/2}$ @1Hz and 3.59pT/Hz$^{1/2}$ @1Hz, respectively. The comparison with Cs-3 data proves the practical performance of the magnetometer.

Based on the completed work, the magnetometer designed in this paper can be further optimized and improved to increase the number of laser beams. If the multi-channel probes under the same light source can work simultaneously, the full-axis magnetic field gradiometer with the same light source can be constructed. In addition, to ensure the quality of magnetic gradient measurement data, according to different application scenarios, magnetic compensation algorithm can be introduced into signal detection and processing system to realize real-time data preprocessing.

REFERENCES

[1] Matzka, J.; Chulliat, A.; Mandea, M.; Finlay, C.C.; Qamili, E. Geomagnetic Observations for Main Field Studies: From Ground to Space. *Space Science Reviews* **2010**, 155, 29–64.

[2] Ichihara S , Mizutani N , Ito Y , et al. Differential Measurement With the Balanced Response of Optically Pumped Atomic Magnetometers[J]. *IEEE Transactions on Magnetics*, 2016, 52(8):1-1..

[3] Zhou, Z.; Wang, C.; Ma, M.; Zeng, F.; Cheng, D.; Ji, Y. Research of control system model and design of digital controller for 4he optically pumped magnetometer (OPM). Journal of Computational and Theoretical Nanoscience **2016**, 13, 43–49.

[4] Schultze, V.; Schillig, B.; Ijsselsteijn, R.; Scholtes, T.; Woetzel, S.; Stolz, R. An optically pumped magnetometer working in the light-shift dispersed Mz mode. *Sensors (Switzerland)* **2017**, 17,561-.

[5] Labyt E, Corsi M C, Fourcault W. Magnetoencephalography With Optically Pumped ⁴He Magnetometers at Ambient Temperature[J]. *IEEE Transactions on Medical Imaging*, **2019**, 38(1):90-98..

[6] Elrefai A L , Sasada I , Harada S . Gradiometer and Magnetometer Integration Using a Pair of Fundamental Mode Orthogonal Fluxgate Sensor Heads[J]. *Magnetics IEEE Transactions on Magnetics*, **2015**, 51(11):1-4..

[7] Sheng D , Perry A R , Krzyzewski S P , et al. A microfabricated optically-pumped magnetic gradiometer[J]. *Applied Physics Letters*, **2017**, 110:031106.

[8] Tobely T E , Salem A . Position detection of unexploded ordnance from airborne magnetic anomaly data using 3-D self organized feature map[C]// *IEEE International Symposium on Signal Processing & Information Technology*. IEEE, **2006**.

[9] Pärkkä, J, Ennes, M, Van Gils, M. Automatic feature selection and classification of physical and mental load using data from wearable sensors[J]. *Information technology & applications in biomedicine IEEE international conferen*, **2010**:1-5.

[10] Pradhan, S.; Mishra, S.; Behera, R.; Poornima; Dasgupta, K. An atomic magnetometer with autonomous frequency stabilization and large dynamic range. *Review of Scientific Instruments* **2015**, 86, 063104.

[11] Leger, J.-M.; Bertrand, F.; Jager, T.; Le Prado, M.; Fratter, I.; Lalaurie, J.-C. Swarm Absolute Scalar and Vector Magnetometer Based on Helium 4 Optical Pumping. *Procedia Chemistry* **2009**, 1, 634–637.

[12] Fratter, I.; Léger, J.-M.; Bertrand, F.; Jager, T.; Hulot, G.; Brocco, L.; Vigneron, P. Swarm Absolute Scalar Magnetometers first in-orbit results. *Acta Astronautica* **2016**, 121, 76–87.

[13] Budker D , Romalis M . Optical magnetometry[J]. *Nature Physics*, **2007**.

[14] Savukov I , Kim Y J , Shah V , et al. High-sensitivity operation of single-beam optically pumped magnetometer in a kHz frequency range[J]. *Measurement Science and Technology*, **2017**, 28:035104.

[15] Plante, M.K.; MacFarlane, D.L.; McGregor, D.D.; Slocum, R.E.; Sampson, W.M.; Brown, A.W. Generalized theory of double-resonance optical pumping of ⁴He. *Physical Review A* **2010**, 82, 013837.

[16] McGregor, D.D. High-sensitivity helium resonance magnetometers. *Review of Scientific Instruments* **1987**, 58, 1067–1076.

[17] Y. Gu, R. Y. Shi, Y. H. Wang. Study on sensitivity-related parameters of distributed feedback laser-pumped cesium atomic magnetometer. *Acta Physica Sinica* **2014**, 63, 1–9.

[18] Chen Chen; Qin Jianan; Zhang Xue; Lin Jun; Wang Yanzhang. Temperature controller for DFB laser utilized in SERF atomic magnetometer. *Infrared and Laser Engineering* **2017**, 45, 1205004.

[19] Denisova, N.; Skudra, A. High-frequency electrodeless discharges in helium. *Plasma Sources Science and Technology* **2004**, 13, 594–599.

[20] Gan, Z. Equivalent-Ion Model of the Mixed Gas Discharge. *2012 Asia-Pacific Power and Energy Engineering Conference* **2012**, 1–4.

[21] Mellinger A , Mellinger O . Breakdown threshold of dielectric barrier discharges in ferroelectrets: where Paschen's law fails[J]. *IEEE Transactions on Dielectrics and Electrical Insulation*, **2011**, 18:43-48.

[22] Yuharu S，Kyohei S，Mohamed M，et al. Impedance Matching Antenna-Integrated High-Efficiency Energy Harvesting Circuit[J]. *Sensors (Switzerland)*,17:1763.

[23] Zeng X , Li Z , Wan J , et al. Embedded Hardware Artificial Neural Network Control for Global and Real-time Imbalance

Current Suppression of Parallel Connected IGBTs[J]. *IEEE Transactions on Industrial Electronics*, **2019**:1-1.

[24] Meshram P M , Kanojiya R G . Tuning of PID controller using Ziegler-Nichols method for speed control of DC motor[C]// *International Conference on Advances in Engineering, Science & Management*. IEEE, **2012**.